Three-Stage Static Power Converter for Battery Charging Feasible for Small Wind Energy Conversion Systems

Herminio Miguel de Oliveira Filho, Demercil de S. Oliveira, Jr., *Senior Member, IEEE*, and Carlos Elmano de Alencar e Silva

***Abstract*—This paper presents the analysis, design, simulation, and experimental results for a three-stage static power converter for battery charging feasible to small wind energy conversion systems. The system employs a boost converter cascaded with a Graetz bridge that allows the implementation of a maximum power point (MPP) tracker and the reduction of the mechanical speed under overvoltage conditions across the batteries. Moreover, a buck converter is connected in series with the boost stage to ensure a constant voltage bus between the aforementioned topologies. Thus, it is possible to extract the maximum power over the entire wind speed range, and battery charging can be realized through conventional techniques. The complete design of the proposed battery charger including power, control, and supervisory circuits is presented and developed, considering a 300-W system, with the possibility of charging battery banks rated at 12 or 24 V. Simulation results are presented to prove the existence of MPPs in the wind generator. Finally, experimental results of the developed prototype required to validate the functionality of the proposed study are presented and discussed.**

***Index Terms*— Battery charging, boost converter, buck converter, maximum power point (MPP), wind energy.**

I. Introduction

In general, autonomous wind energy conversion systems use some sort of energy storage device. It can be accomplished by either using batteries to supply electrical equipment (directly or through the dc link of the inverter stage) or gravitational energy methods. The systems that use batteries demand an electronic circuit to control the charging and discharging process of the battery bank.

The direct connection of a three-phase rectifier to batteries is a common practice adopted by some manufacturers. Although there is simplicity and robustness, several problems associated with this solution result [1], such as the reduction of battery useful life and increase of power losses.

In order to solve these problems, many alternative solutions are presented, such as the association of a buck converter in series with a Graetz bridge to extract the maximum power of the turbine [2], [3]. However, this topology does not deliver power to load when the generated peak voltage is less than the battery voltage. Other solution is to use a boost converter in parallel with the Graetz bridge to regulate the input voltage of the battery charger, while the generated voltage is not able to forward bias the rectifier diodes [1]. Moreover, such method does not allow tracking the maximum power for medium and high wind speeds. A simple structure to solve the previous problems is to use a boost converter cascaded with the Graetz bridge [4]. Although this topology operates over the entire range of wind speed, this practice is not usual due to the necessity of high voltages, i.e., many batteries in series. The buck–boost converter is another topology already studied in [5] and [6], but its disadvantage lies in the reversed output voltage. The use of semicontrolled rectifiers as in [7] and [8] represents good solutions to improve the power factor in electrical machines, but the inclusion of extra switches and current sensors may cause the battery charger cost to increase significantly. Pulse-width modulation (PWM) rectifiers are also a prominent solution [9], [10], but they are more appropriated in medium and large systems due to high implementation cost.

The converter feasible to small wind energy conversion systems (SWECSs) proposed in this paper tries to aggregate the main advantages existent in the aforementioned topologies, which consist in uncontrolled rectifiers cascaded with dc–dc converters. The proposed battery charger shown in Fig. 1 presents a Graetz bridge associated with a boost converter and a buck converter. The Graetz bridge is used to rectify the ac generated voltage. The boost converter is responsible for tracking the maximum power through a maximum power point (MPP) tracker (MPPT) system over the full range of wind speed. It is also responsible for regulating the battery bank voltage, thus reducing the permanent-magnet synchronous generator (PMSG) rotation due to high voltage levels that may appear across the

Manuscript received August 28, 2013; revised December 27, 2013; accepted February 4, 2014. Date of publication March 4, 2014; date of current version September 16, 2014. Paper 2013-SECSC-643.R1, presented at the 2012 IEEE/IAS International Conference on Industry Applications, Fortaleza, Brazil, November 5–7, and approved for publication in the IEEE Transactions on Industry Applications by the Sustainable Energy Conversion Systems Committee of the IEEE Industry Applications Society. This work was supported by the Coordenação de Aperfeiçoamento de Pessoal de Nível Superior (CAPES).

H. M. de Oliveira Filho is with the Institute for Engineering and Sustainable Development (IEDS), University for the International Integration of the Afro-Brazilian Lusophony (UNILAB), Acarape 62785-000, Brazil (e-mail: herminio@unilab.edu.br).

D. de S. Oliveira, Jr. is with the Group of Power Processing and Control (GPEC), Electrical Engineering Department, Federal University of Ceará (UFC), Fortaleza 60455-760, Brazil (e-mail: demercil@dee.ufc.br).

C. E. de Alencar e Silva is with the Computer Engineering Undergraduate Course, Federal University of Ceará (UFC), Sobral 62010-560, Brazil (e-mail: elmano@sobral.ufc.br).

Color versions of one or more of the figures in this paper are available online at http://ieeexplore.ieee.org.

Digital Object Identifier 10.1109/TIA.2014.2309723

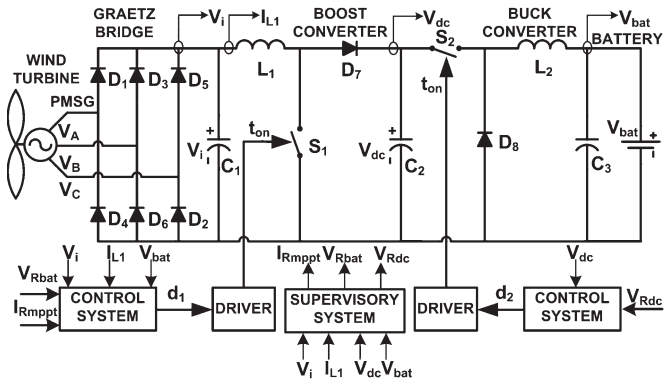

Fig. 1. Proposed battery charger.

TABLE I
SPECIFICATIONS FOR THE DESIGN EXAMPLE

Generated power (P_g)	350 W
Rectified input voltage (V_i)	45 V
DC link voltage (V_{dc})	70 V
Maximum output voltage (V_{bat})	28.8 V
Maximum output current (I_{bat})	30 A

battery. Finally, the buck converter is used to control the dc link in order to ensure constant voltage and the adequate interconnection of the aforementioned converters. Moreover, the number of batteries connected to the battery charger can be properly adjusted. The disadvantage of the proposed topology is the use of many cascaded converters, leading to the reduction of the global efficiency of the battery charger. The design of the proposed three-stage static power converter is presented, so that simulation and experiment can be obtained and properly discussed to validate the theoretical study.

II. DESIGN EXAMPLE

The proposed battery charger feasible to SWECSs shown in Fig. 1 is composed of a triblade horizontal-axis wind turbine (HAWT) emulated with ratio and power coefficient equal to 0.505 m and 0.48, respectively. The HAWT is connected to an axial flux PMSG, known as Torus machine, which is rated at 350 W for the generated power, generated peak voltage of 45 V, 14 poles, and electrical frequency of about 60 Hz. The battery bank is composed of one or two lead–acid batteries, both rated at 12 V/150 Ah. A design example for the battery charger is presented as follows.

A. Power Stage

The power stage design considers the specifications shown in Table I and the assumptions given in Table II. From the aforementioned data and by using the methods proposed in [11] and [12], the values obtained for the filter elements are presented in Table III. For the choice of the capacitors, the equivalent series resistance and rms current were used as key parameters.

The semiconductors were chosen according to the design procedure and properly considering both current and voltage stresses according to the availability of components in the laboratory. Diodes 1N5408 are used as rectifier diodes, MBR100C20 corresponds to the Schottky diodes in the dc–dc converters, and MOSFETs IRFP4710 are the main switches.

TABLE II
ASSUMPTIONS FOR THE DESIGN EXAMPLE

Efficiency for each converter (η)	0.95
Switching frequency for each converter f_s	20 kHz
Input voltage ripple (ΔV_i)	15%
Inductor L_1 current ripple (ΔI_{L1})	10%
Dc link voltage ripple (ΔV_{dc})	5%
Output voltage ripple (ΔV_{bat})	4%
Inductor L_2current ripple (ΔI_{L2})	10%

TABLE III
VALUES OBTAINED FOR FILTER ELEMENTS

Graetz bridge capacitance (C_1)	5 mF
Boost inductance (L_1)	1 mH
Boost capacitance (C_2)	750 μF
Buck inductance (L_2)	156 μH
Buck capacitance (C_3)	2 mF

B. Control System

The control system aims to limit the battery voltage through the reduction of the mechanical speed of the wind turbine and also implement the MPPT system.

Fig. 2 shows the block diagram that represents the control system in the boost stage. The structure is similar to that proposed in [4], but it is used to regulate the battery voltage. The internal controller $C_{\mathrm{IL1}}(s)$ regulates the average inductor current I_{L1} considering the variation of the duty cycle d_1. The reference signal I_{ref} for this compensator is the highest signal between the MPPT reference current I_{MPPT} and the control signal I_{CVi} provided by the input voltage controller. If the battery bank voltage does not present overvoltage, the reference for the average inductor current would be the optimal current that allows obtaining the MPP. Otherwise, the reference will be provided by an external loop controller $C_{\mathrm{Vbat}}(s)$. This control signal is supposed to be decreased so that the wind turbine slows down as well as the input voltage V_i decreases and the battery voltage can be regulated. Thus, it is possible to optimize the power delivery and implement a protection system for the batteries at the same time.

Fig. 3 shows the block diagram for the control system of the buck stage. By using controller $C_{\mathrm{Vdc}}(s)$, the buck converter duty cycle is adjusted to maintain the dc-link voltage V_{dc} high and constant, consequently ensuring the correct interaction between the boost and buck converters.

The transfer functions (TFs) of the controlled plants are modeled by using the instantaneous average-value method [12]. The control system was designed according to the guidelines given in [12] and [13]. The boost stage control system is composed of three controllers, i.e., a proportional-integrator (PI) controller with filter, a PI controller, and an integrator. To control the dc-link voltage in the buck converter, a proportional–integral–derivative controller is employed.

The conditions adopted to design the controllers are to obtain a compensated loop gain with a slope of -20 dB/dec at the desired crossover frequency to ensure stability to the system and phase margin higher than 45° to avoid dynamic behavior with high oscillations.

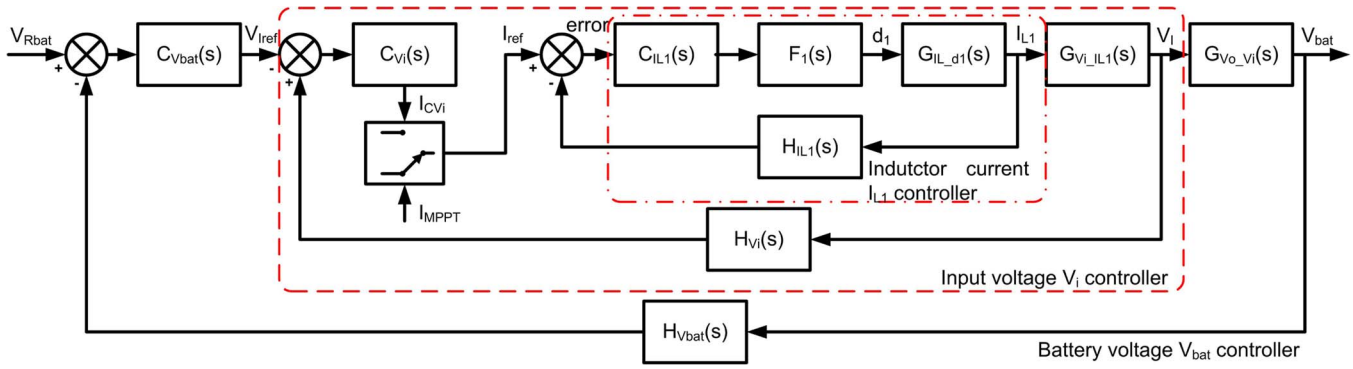

Fig. 2. Block diagram representing the control system used in the boost stage.

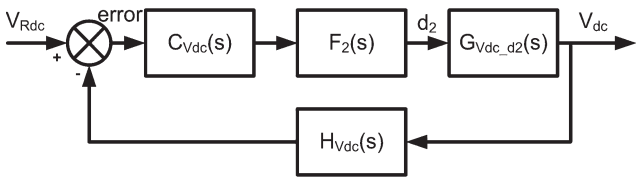

Fig. 3. Block diagram representing the control system used in the buck stage.

1) Control of Average Inductor Current I_{L1}: The instantaneous average value for inductor voltage (1) is obtained replacing the voltages according to each operation step, i.e., the duty cycle $d_1(t)$ for switch S_1 and its complement $d_1'(t)$. To construct a small-signal ac model at a quiescent operating point, one assumes that $\langle i_{L_1}(t)\rangle$ and $\langle v_i(t)\rangle$ are equal to some given constant values I_{L1} and D_1, increased by some superimposed small ac variations $\hat{i}_{L_1}(t)$ and $\hat{d}_1(t)$, as shown in (2) and (3). Replacing (2) and (3) in (1), the expression is linearized, eliminating dc and second-order ac terms. Using the Laplace transform, the TF is obtained in (4) considering perturbations only in the inductor current $i_{L1}(s)$ and duty cycle $d_1(s)$. The remaining magnitudes are considered as time invariant. The plant for the aforementioned control system is constituted by (4) and the PWM modulator, whose TF is represented by $F_1(s) = 1/V_m$, where V_m is the amplitude of the sawtooth carrier

$$L_1 \frac{d\langle i_{L_1}(t)\rangle_{T_{S_1}}}{dt} = \left(\langle v_i(t)\rangle_{T_{S_1}}\right) d_1(t) + \left(\langle v_i(t)\rangle_{T_{S_1}} - V_{\rm dc}\right) d_1'(t) \quad (1)$$

$$\langle i_{L_1}(t)\rangle_{T_{S_1}} = I_{L_1} + \hat{i}_{L_1}(t) \quad (2)$$

$$d_1'(t) = D_1' + \hat{d}_1(t) \quad (3)$$

$$G_{I_{L1-d_1}}(s) = \frac{\hat{i}_{L_1}(s)}{\hat{d}_1(s)} = \frac{V_{\rm dc}}{s \cdot L_1}. \quad (4)$$

The compensator, shown in (5), was designed to adjust the crossover frequency at one decade (2 kHz) below the switching frequency. According to the classic control theory, the crossover frequency of a controlled system cannot be higher than one quarter of the rated frequency of the plant [14]. This procedure is necessary to avoid the mitigation of the plant natural oscillation by the compensator, which makes the system unstable

$$C_{i_{L_1}}(s) = 1.1 \cdot \frac{s + 1.2 \times 10^3}{s \cdot (s + 6.8 \times 10^4)}. \quad (5)$$

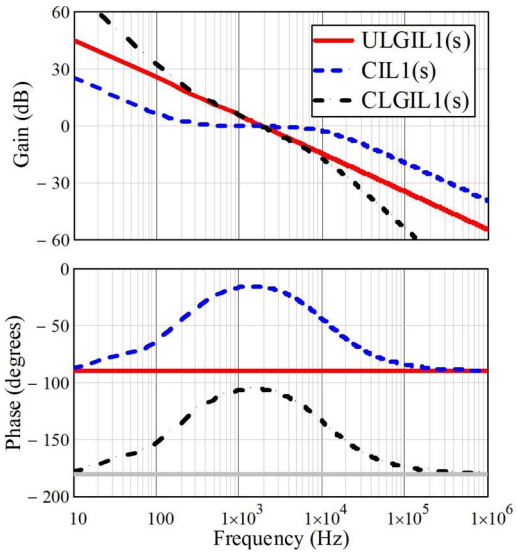

Fig. 4. Bode diagrams for $\mathrm{UCL}_{\mathrm{IL1}}(s)$, $C_{\mathrm{IL1}}(s)$, and $\mathrm{CLG}_{\mathrm{IL1}}(s)$.

The Bode plots for the gain and phase of the uncompensated loop $\mathrm{ULG}_{\mathrm{IL1}}(s)$, the compensator $C_{\mathrm{IL1}}(s)$, and the compensated loop $\mathrm{CLG}_{\mathrm{IL1}}(s)$ are shown in Fig. 4. The obtained phase margin is equal to 74° with a slope of −20 dB/dec at the crossover frequency.

2) Control of Input Voltage V_i: The method used to obtain the TF of the system in (6) is the similar to previous one. The TF is obtained considering perturbations only in the input voltage $v_i(s)$ and inductor current $i_L(s)$. This plant has a slow dynamic, and duty cycle variations are not so influent, as it can be considered constant. The dc-link voltage $V_{\rm dc}$ is regulated by the buck control system, and the input capacitor series resistance R_{C1} is considered in this plant because it affects the input voltage ripple. The variation of the input voltage influences the mechanical speed, while the inertia moment J must be included in the dynamic model. The equivalent inertia was obtained by energy equivalence and is represented by capacitor C_J in (7). If the generator current dynamic is ignored, C_J can be considered in parallel with C_1. The system considered in this control system is formed by (6) and the closed-loop TF $\mathrm{CLTF}_{\mathrm{IL1}}(s)$ obtained in (4).

The compensator is presented in (8), and it was designed to adjust the crossover frequency at one quarter (15 Hz) of the natural frequency of the plant, i.e., the generated electrical

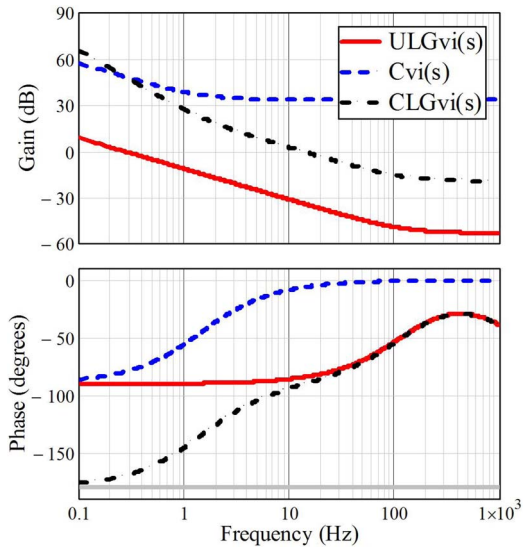

Fig. 5. Bode diagrams for $\mathrm{ULG}_{Vi1}(s)$, $C_{Vi}(s)$, and $\mathrm{CLG}_{Vi}(s)$.

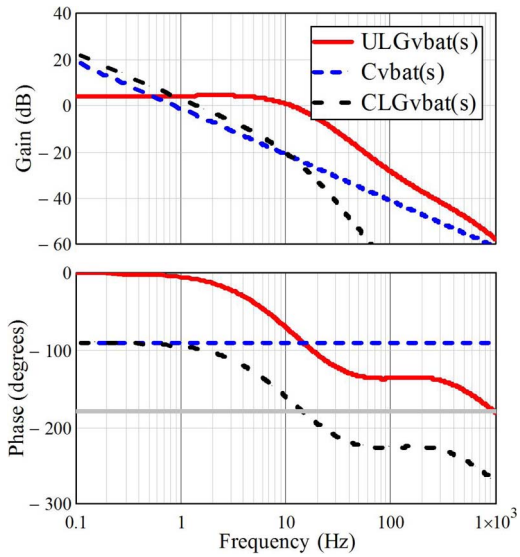

Fig. 6. Bode diagrams for $\mathrm{ULG}_{\mathrm{Vbat}}(s)$, $C_{\mathrm{Vbat}}(s)$, and $\mathrm{CLG}_{\mathrm{Vbat}}(s)$.

frequency in this case. Moreover, the crossover frequency cannot be higher than one quarter of the crossover frequency of the internal closed loop to ensure the decoupling between the controlled plants and, consequently, stability and absence of oscillations

$$G_{V_i-I_{L1}}(s)=\frac{\hat{v}_i(s)}{\hat{i}_{L_1}(s)}=-R_{C_1}\cdot\frac{s+\frac{1}{R_{C_1}\cdot C_1'}}{s} \tag{6}$$

$$C_1'=C_1+C_J=C_1+J\cdot\frac{\omega_m^2}{V_i^2} \tag{7}$$

$$C_{v_1}(s)=54.6\cdot\frac{s+9.2}{s}. \tag{8}$$

The Bode plots for the uncompensated loop $\mathrm{ULG}_{Vi}(s)$, the compensator $C_{Vi}(s)$, and the compensated loop $\mathrm{CLG}_{Vi}(s)$ are presented in Fig. 5. The obtained phase margin is equal to 91° with a slope of −20 dB/dec at the crossover frequency.

3) Control of Battery Voltage V_{bat}: To obtain the TF of the plant in (9), only perturbations in the output voltage $v_{\mathrm{bat}}(s)$ and input voltage $v_i(s)$ are considered. This plant has slow dynamic, while duty cycle variations are barely noticeable. The dc-link voltage V_{dc} is constant due to the buck stage control system. The battery is modeled as an internal resistance R_{bat} in series with a capacitance C_{bat}, which is obtained in (10). The plant for this control system is formed by (9) and the closed-loop TF $CLTF_{Vi}(s)$ obtained in (6).

The compensator is presented in (11), and it was designed to adjust the crossover frequency at one decade (1.5 Hz) below the crossover frequency of the internal closed loop due to the aforementioned reasons

$$G_{V_{\mathrm{bat}}-V_i}(s)=\frac{\hat{v}_{\mathrm{bat}}(s)}{\hat{v}_i(s)}=\frac{\alpha\left(s+\frac{1}{R_{\mathrm{bat}}C_{\mathrm{bat}}}\right)}{s^3+\frac{C_3+C_{\mathrm{bat}}}{R_{\mathrm{bat}}C_3C_{\mathrm{bat}}}s^2+\frac{1}{\alpha}s+\frac{1}{\alpha R_{\mathrm{bat}}C_{\mathrm{bat}}}} \tag{9}$$

where $L_e=L_1//L_2$ and $\alpha=1/L_eC_3$.

$$C_{\mathrm{bat}}=\frac{3600\cdot\mathrm{Cap}_{\mathrm{Ah}}}{N\cdot V_{\mathrm{bat}}} \tag{10}$$

where $\mathrm{Cap}_{\mathrm{Ah}}$ is the battery capacity and N is the number of batteries

$$C_{v_{\mathrm{bat}}}(s)=0.6\cdot\frac{1}{s}. \tag{11}$$

The Bode plots for the uncompensated loop $\mathrm{ULG}_{\mathrm{Vbat}}(s)$ considering one or two batteries are similar, while this example was designed for two units. The Bode plots for $\mathrm{ULG}_{\mathrm{Vbat}}(s)$, the compensator $C_{\mathrm{Vbat}}(s)$, and the compensated loop gain $\mathrm{CLG}_{\mathrm{Vbat}}(s)$ are presented in Fig. 6. The obtained phase margin is equal to 81° with a slope of −20 dB/dec at the crossover frequency.

4) Control of DC-Link Voltage V_{dc}: Finally, the TF of the plant is presented in (12), which is obtained considering only perturbations in the dc-link voltage $v_{\mathrm{dc}}(s)$ and the buck stage duty cycle $d_2(s)$. The output voltage is stabilized by the boost stage control system, and the input capacitor series resistance R_{C2} is considered due to the same aforementioned issues.

The plant for the control system is formed by (12) and the PWM modulator, whose TF is $F_2(s)$.

The compensator, shown in (13), was designed for a crossover frequency of 20 times (1 kHz) less than the switching frequency of the buck converter

$$G_{V_{\mathrm{dc}}-d_2}(s)=\frac{\hat{v}_{\mathrm{dc}}(s)}{\hat{d}_2(s)}=-I_{\mathrm{dc}}R_{C_2}\frac{\left(s+\frac{1}{R_{C_2}C_2}\right)\left(s+\frac{D_2V_{\mathrm{dc}}}{I_{\mathrm{dc}}L_2}\right)}{s^2+\frac{R_{C_2}D_2^2}{L_2}s+\frac{D_2^2}{L_2C_2}} \tag{12}$$

$$C_{i_{L_1}}(s)=6.6\cdot\frac{(s+439.9)\cdot(s+439.9)}{s\cdot(s+2.2\times10^3)}. \tag{13}$$

The Bode plots for the uncompensated loop $\mathrm{ULG}_{\mathrm{Vdc}}(s)$, the compensator $C_{\mathrm{Vdc}}(s)$, and the compensated loop $\mathrm{CLG}_{\mathrm{Vdc}}(s)$ are presented in Fig. 7. The obtained phase margin is equal to 92° with a slope of −20 dB/dec at the crossover frequency.

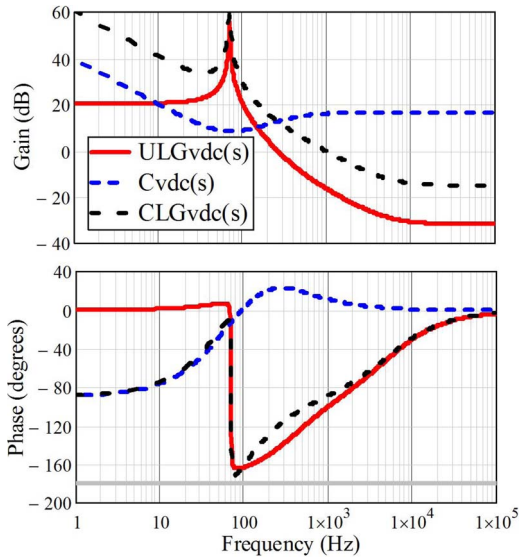

Fig. 7. Bode diagrams for $\mathrm{ULG}_{\mathrm{Vdc}}(s)$, $C_{\mathrm{Vdct}}(s)$, and $\mathrm{CLG}_{\mathrm{Vdc}}(s)$.

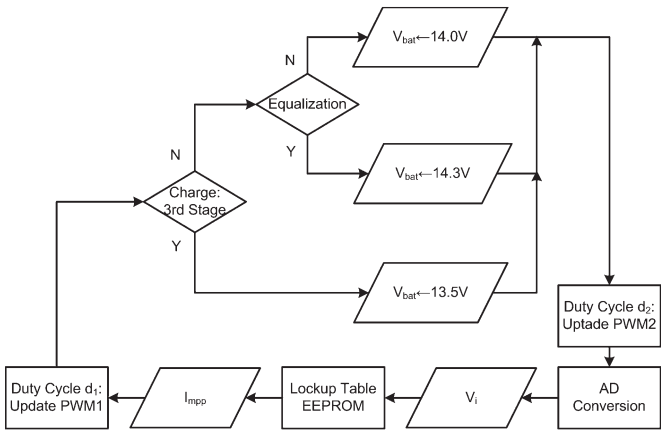

Fig. 8. Flowchart for the adjustment of the reference levels.

C. Supervisory System

The supervisory system, which was developed using Microchip PIC16F877A, gives the set point for the control system and comprises two main functions: providing the output voltage reference and also the MPP reference. Other functions for the supervisory system are monitoring of the charging state, choice of the battery charging mode (charge or equalization), and self-adjustment of the output voltage references according to the number of batteries connected to the converter.

The main function of the implemented algorithm is basically to set the initial configurations of core and memories of the microcontroller such as internal fuses, libraries, and peripheral devices [electrically erasable programmable read-only memory (EEPROM), I/O ports, A/D converters, timers, and PWM channels]. Moreover, it is supposed to check the number of batteries connected to the charger, i.e., one or two units. The set points are adjusted in an interruption routine and provided by PWM signals with RC passive filters.

The flowchart of the interruption routine, which provides the references for the controllers, is shown in Fig. 8. The first function of the routine is to provide the voltage set point,

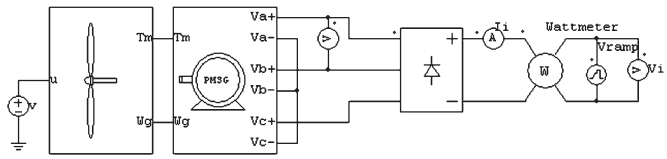

Fig. 9. Electric circuit simulated to obtain the MPP.

which has priority because it is necessary to preserve battery useful life due to overvoltage. It regulates the converter through the operation of the wind turbine out of the MPP region and develops a modified three-stage charging method (limited current, constant charging voltage, and constant floating voltage) with equalization mode. The limit for the output voltage is recommended by the battery manufacturer (14.0 V for charging and 14.3 V for equalization). When the battery voltage reaches the limit and the current through the battery is minimum (at 2% of capacity), the charging reaches the third stage, as the output voltage is set to the floating point (13.5 V). The second function consists in regulating the optimum average inductor current of the boost converter according to the measured input voltage V_i so that the wind generator operates at MPP using a lookup table recorded in the internal EEPROM of the microcontroller.

III. Simulation Results

Simulation tests were performed in order to evaluate the proposed system model. All simulations of the system under study are realized using the PSIM software.

In this paper, the simulations are focused on the determination of the MPPs by adding a controlled voltage supply in the output of the rectifier, as shown in Fig. 9. The controlled voltage supply determines a variation in ramp form for the input voltage V_i. This variation changes the impedance seen by the generator and, consequently, the generated voltage. The mechanical speed is then changed according to the variation of the generated voltage. Hence, by observing the output power waveform, one can verify the existence of a point at which the output power is maximum. This MPP occurs at an optimal dc-link voltage for each value of the wind speed [1].

Fig. 10 shows the output power curve, where the wind speed is 12 m/s and the dc-link voltage was varied from 0 to 80 V in the ramp form during the simulation. It is observed that the maximum power is 345 W, occurring at an input voltage of about 43.7 V. Therefore, this value is the optimal point for the simulated wind speed.

It is also worth to mention that there is a significant power waste if the MPPT system is not included, as shown in Fig. 10. It is observed that, for the floating battery bank voltages of 13.5 and 27 V, the transferred output powers are nearly 30 and 240 W, respectively. It means that appreciable power losses will exist in the electric machine if a system composed of the wind generator and the rectifier supplies the battery bank directly.

Fig. 11 shows the simulation results for the MPP over a wide range of the wind speed. In the battery charger prototype, for each sampled value of the input voltage, an optimal reference current for the inductor current controller is set in accordance with the data recorded in the EEPROM of the microcontroller.

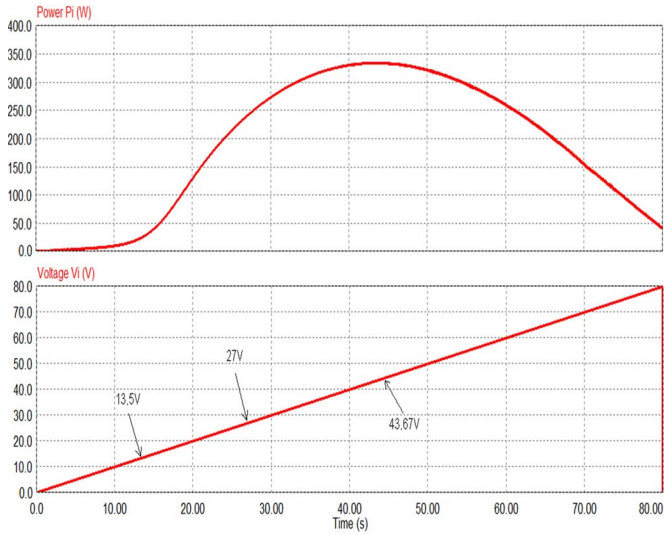

Fig. 10. Profile of the extract power when the input voltage across the rectifier stage varies in the ramp form for $v = 12$ m/s.

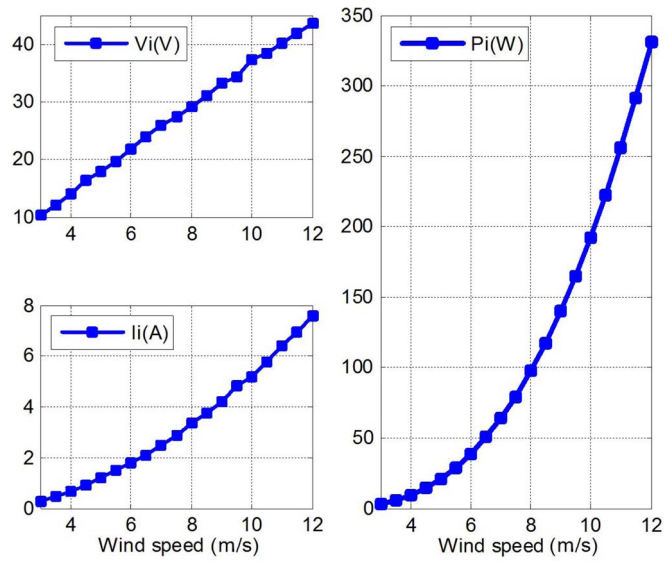

Fig. 11. Simulation results with MPP operation.

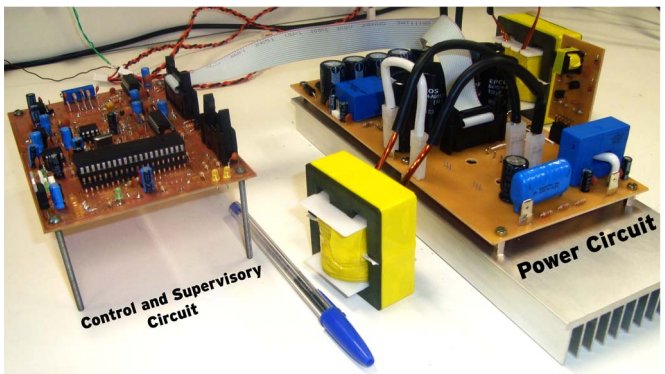

Fig. 12. Experimental prototype of the battery charger.

IV. Experimental Results

Fig. 12 shows the implemented prototype, composed of control, supervisory, and power processing circuitries. The experimental results focus on three main aspects: steady state, dynamic behavior (MPPT and battery voltage regulation modes), and efficiency.

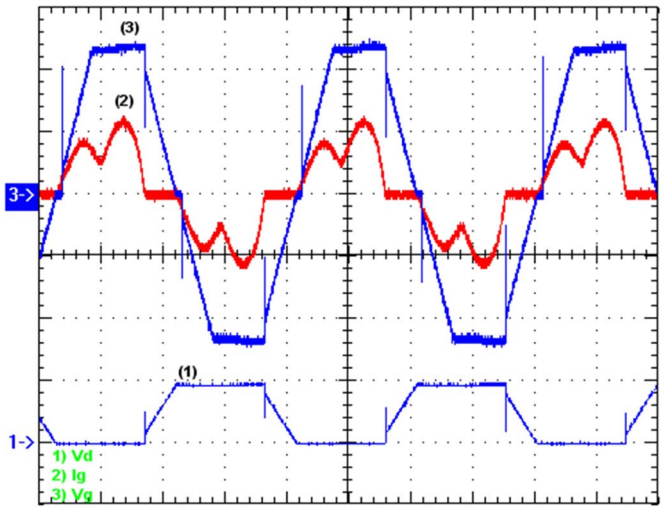

Fig. 13. (1) Line voltage V_L (20 V/div). (2) Line current I_L (10 A/div). (3) Rectified voltage V_d (50 V/div). Time base: 4 ms/div.

The PMSG is driven using a dc machine and a variable voltage source in series with a resistive bank to regulate the armature voltage. Thus, it is possible to emulate a wind turbine and also the wind speed. The machine is rated at 220 V/9.1 A/1800 r/min, and the voltage source is rated at 550 V/15 A.

A. Steady-State Behavior

The results in steady-state condition were obtained using one battery as load. Fig. 13 shows the generated line voltage, the line current, and the rectified voltage. The line voltage and line current waveforms present the typical nonlinear shape of a Torus machine connected to a three-phase rectifier. The rms and maximum line voltage values are 35.5 and 46 V, respectively, while the maximum line current is 11.7 A.

The waveforms for input voltage V_i, inductor current I_{L1}, dc-link voltage $V_{\rm dc}$, and battery current $I_{\rm bat}$ are shown in Fig. 14. It can be seen that V_i (45 V) and I_{L1} (7.6 A) and their respective ripples remain within the limits of the design example. The dc-link voltage $V_{\rm dc}$ equals 68.5 V, and the error is about 3.5% when compared with the assumption for the design (70 V). Analogously, Fig. 14 shows the battery current, while the average value is 21.5 A and the current ripple is not higher than the design specification. The maximum rated value for $I_{\rm bat}$ (28.5 A) is not reached because the battery is in half-charge state.

B. Dynamic Tests

The results regarding the dynamics of the proposed system were obtained using two batteries as load. The MPPT operation mode is shown in Fig. 15. A discrete variation of the current through the inductor for a continuous input voltage variation is observed. It occurs because the MPPT algorithm used in the prototype is based on a lookup table. Since the bus voltage $V_{\rm dc}$ is constant, the battery current presents a similar shape.

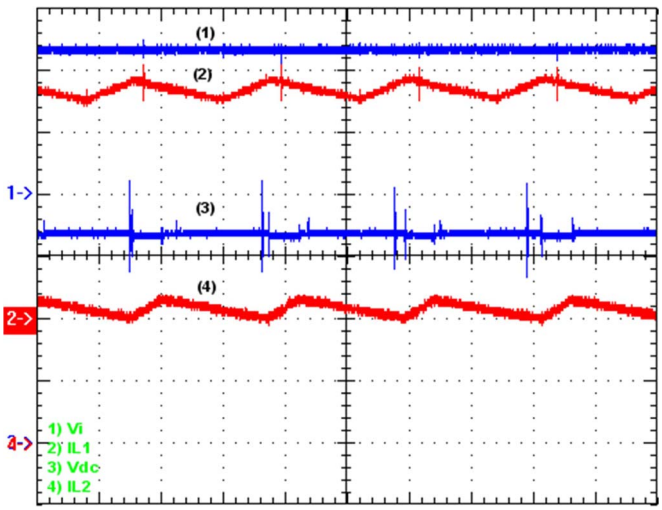

Fig. 14. (1) Input voltage V_i (20 V/div). (2) Inductor current I_{L1} (2 A/div). (3) DC-link voltage $V_{\rm dc}$ (20 V/div). (4) Battery current I_{L2} (10 A/div). Time base: 20 μs/div.

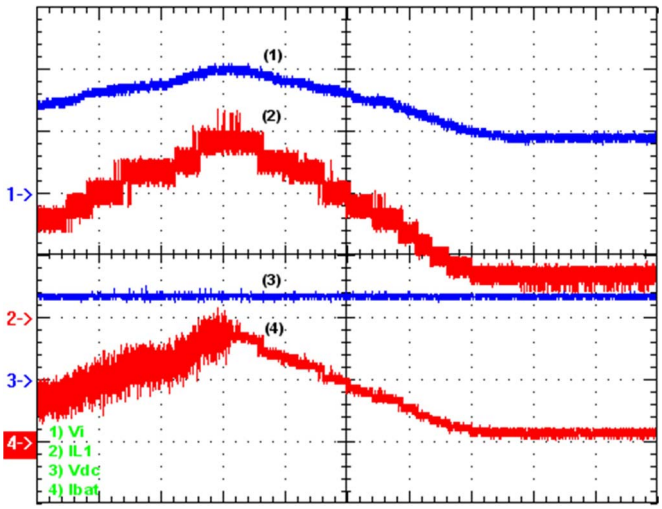

Fig. 15. (1) Input voltage V_i (20 V/div). (2) Inductor current I_{L1} (2 A/div). (3) DC-link voltage $V_{\rm dc}$ (50 V/div). (4) Battery current $I_{\rm bat}$ (5 A/div). Time base: 1 s/div.

To verify if the MPPT mode performs correctly, the mechanical speed of the dc machine was varied to obtain the values for the input voltage and current through the inductor. Therefore, it is possible to compare simulated and experimental results. The results are presented in Fig. 16, as it is possible to observe that the current through the inductor and the input power present small error when compared with the values in Fig. 11. The only exceptions are the first two results, which represent negligible values. It occurs due to the high static gain of the boost stage at small wind speeds, causing the operation of the converter in discontinuous conduction mode. The results for input power are shown in Fig. 17, and it is observed that experimental results are similar to simulation realized.

Fig. 18 shows the battery voltage $V_{\rm bat}$ and the current through battery bank $I_{\rm bat}$ for the voltage regulation operation mode. The battery voltage reference was chosen to regulate the battery bank voltage around the floating point, defined as 25.0 V (i.e., 12.5 V per battery). It is observed that the control

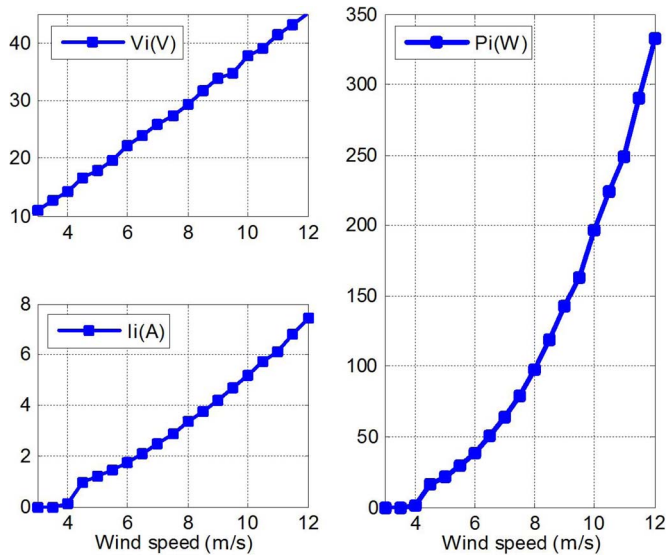

Fig. 16. Experimental results with MPP operation.

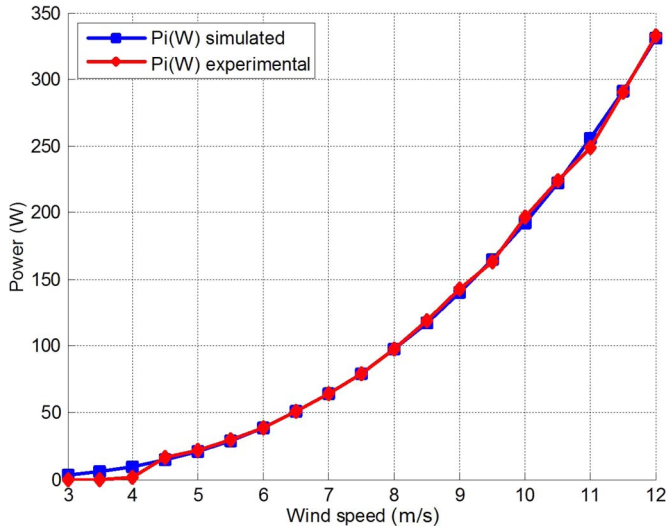

Fig. 17. Simulated and experimental results of input power P_i with MPP operation.

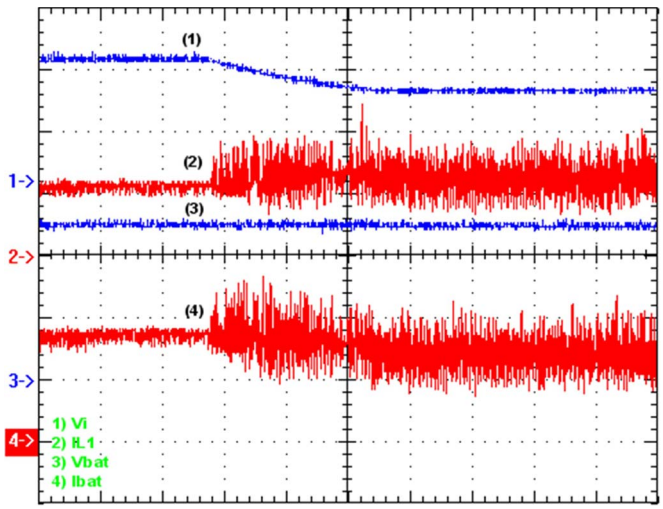

Fig. 18. (1) Input voltage $V_{\rm dc}$ (20 V/div). (2) Inductor current I_{L1} (2 A/div). (3) Battery voltage $V_{\rm bat}$ (10 V/div). (4) Battery voltage $I_{\rm bat}$ (5 A/div). Time base: 4 s/div.

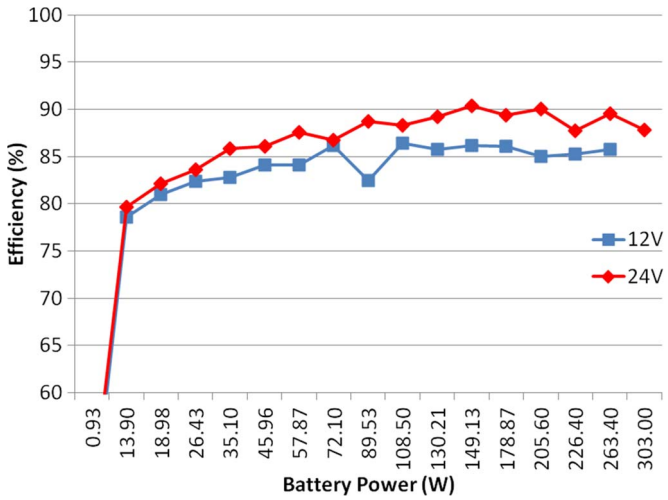

Fig. 19. Measured efficiency of the battery charger as a function of the output power.

system response at a given instant actuates to reduce the current level. The input voltage V_i is decreased, as shown in Fig. 18, and so is the machine rotation. The current through inductor I_{L1} becomes more oscillatory than it was (due to the existence of a low-frequency component), because the battery and input voltage compensators force the current reference to maintain the battery voltage level constant. Moreover, there is the absence of an electronically controlled turbine emulator, which is desirable to ensure the mechanical speed and torque characteristics.

C. Efficiency

Fig. 19 represents the measured efficiency curve of the battery charger as a function of the output power for the battery banks rated at 12 and 24 V, while the respective efficiencies at the rated power are 85.4% and 87.7% and considered satisfactory for low-power stand-alone mode applications. When the system operates with one battery, the output current is doubled, and the stresses involving the buck converter semiconductors are increased, causing the efficiency to decrease.

V. Conclusion

This paper has presented a three-stage battery charger feasible to small wind systems. The operation modes of the proposed system (MPPT and battery voltage regulation) were tested, and acceptable experimental results were obtained.

Although the battery charger is formed by a three-stage static power converter, the prototype presents good efficiency over the entire load range, particularly in the case of two-battery operation.

The developed prototype is an interesting and low-cost choice when it is desirable to transfer the maximum power from the wind turbine to the battery bank over the entire wind speed range and also in cases where it is necessary to vary the number of connected batteries.

Future perspectives for additional studies include the development of perturb-and-observe MPPT algorithms and the use of a variable dc-link $V_{\rm dc}$ voltage according to the generated power, so that faster dynamic response is achieved and the system operates adequately at low wind speeds.

Acknowledgment

The authors would like to thank the Coordenação de Aperfeiçoamento de Pessoal de Nível Superior (CAPES) for the financial support, and also the members of the Group of Power Processing and Control (GPEC) for the friendship and overall support.

References

[1] I. R. Machado, H. M. Oliveira Filho, L. H. S. C. Barreto, and D. S. Oliveira, Jr., "Wind generation system for charging batteries," in *Proc. COBEP*, 2007, pp. 371–376.
[2] E. Koutroulis and K. Kalaitzakis, "Design of a maximum power tracking system for wind-energy-conversion applications," *IEEE Trans. Ind. Electron.*, vol. 53, no. 2, pp. 486–494, Apr. 2006.
[3] K. Y. Lo, Y. M. Chen, and Y. R. Chang, "MPPT battery charger for stand-alone wind power system," *IEEE Trans. Power Electron.*, vol. 26, no. 6, pp. 1631–1638, Jun. 2011.
[4] R. P. T. Bascopé *et al.*, "Electronic circuit for stand-alone wind energy conversion system," in *Proc. COBEP*, 2011, pp. 964–971.
[5] T. Tafticht, K. Agbossou, A. Cheriti, and M. L. Doumbia, "Output power maximization of a permanent magnet synchronous generator based stand alone wind turbine," in *Proc. IEEE ISIE*, 2006, pp. 2412–2416.
[6] S. M. R. Kazmi, H. Goto, H. J. Guo, and O. Ichinokura, "A novel algorithm for fast and efficient speed-sensorless maximum power point tracking in wind energy conversion systems," *IEEE Trans. Ind. Electron.*, vol. 58, no. 1, pp. 29–36, Jan. 2011.
[7] D. S. Oliveira, Jr., M. M. Reis, L. H. S. C. Barreto, F. L. M. Antunes, and B. L. Soares, "A three-phase high-frequency semicontrolled rectifier for PM WECS," *IEEE Trans. Power Electron.*, vol. 25, no. 3, pp. 677–685, Mar. 2010.
[8] B. R. de Almeida and D. S. Oliveira, Jr., "Control system vertical-axis WECS," in *Proc. COBEP*, 2011, pp. 825–830.
[9] A. Mirecki, X. Roboam, and F. Richardeau, "Architecture complexity and energy efficiency of small wind turbines," *IEEE Trans. Ind. Electron.*, vol. 54, no. 1, pp. 660–670, Feb. 2007.
[10] G. Gamboa, C. Hamilton, J. Baker, M. Pepper, and I. Batarseh, "A unity power factor, maximum power ponit tracking battery charger for low power wind turbines," in *Proc. IEEE APEC Expo.*, 2010, pp. 143–148.
[11] M. H. Rashid, *Power Eletronics: Circuits, Devices and Applications,* 3rd ed. Upper Saddle River, NJ, USA: Prentice-Hall, 2004, pp. 103–110.
[12] R. W. Erickson and D. Maksimovic, *Fundamentals of Power Electronics,* 2nd ed. Boston, MA, USA: Kluwer, 2004, pp. 17–29.
[13] W. Tang, F. C. Lee, and R. B. Ridley, "Small-signal modeling of average current-mode control," *IEEE Trans. Power Electron.*, vol. 8, no. 2, pp. 112–119, Apr. 1993.
[14] K. Ogata, *Modern Control Engineering,* 5th ed. Upper Saddle River, NJ, USA: Prentice-Hall, 2009.

Herminio Miguel de Oliveira Filho was born in Taguatinga, Brazil, in 1983. He received the B.Sc. and M.Sc. degrees in electrical engineering from the Federal University of Ceará (UFC), Fortaleza, Brazil, in 2007 and 2010, respectively, where he is currently working toward the Ph.D. degree in the Group of Power Processing and Control (GPEC), Electrical Engineering Department.

He is currently a Professor with the University for the International Integration of the Afro-Brazilian Lusophony (UNILAB), Acarape, Brazil. His interest areas include control applications in power electronics, microcontrolled systems, switched-mode power supplies, dc–dc conversion, and renewable energy applications.

Demercil de S. Oliveira, Jr. (SM'13) was born in Santos, Brazil, in 1974. He received the B.Sc. and M.Sc. degrees in electrical engineering from the Federal University of Uberlândia, Uberlândia, Brazil, in 1999 and 2001, respectively, and the Ph.D. degree from the Federal University of Santa Catarina, Florianopolis, Brazil, in 2004.

He is currently a Researcher with the Group of Power Processing and Control (GPEC), Electrical Engineering Department, Federal University of Ceará (UFC), Fortaleza, Brazil. His interest areas include static power converters, soft commutation, and renewable energy applications.

Carlos Elmano de Alencar e Silva was born in Fortaleza, Brazil, in 1981. He received the B.S., M.Sc., and Ph.D. degrees in electrical engineering from the Federal University of Ceará (UFC), Fortaleza, in 2004, 2007, and 2012, respectively.

He is currently a Professor of undergraduate and graduate courses in electrical engineering and computer engineering with UFC, Campus Sobral. His interest areas include ac–dc conversion with high power factor, dc–ac conversion, and renewable energy applications.